

# Numerical modeling of spatial profiles of geomagnetically induced electric field intensity in and around Japan

by

Shigeru FUJITA<sup>1,2</sup>, Ikuko FUJII<sup>1</sup>, Arata ENDO<sup>3</sup> and Hiroki TOMINAGA<sup>4</sup>

<sup>1</sup>Meteorological College

<sup>2</sup>National Institute of Polar Research

<sup>3</sup>Global Environment and Marine Department, Japan Meteorological Agency

<sup>4</sup>Tokyo Regional Headquarters, Japan Meteorological Agency

Received 27 November 2017; accepted 14 December 2017;  
published 23 March 2018

## Abstract

The nationwide intensity map of geomagnetically induced electric fields (GIEs) in Japan is presented by using a numerical modeling method. We estimate near-surface resistivity distributions from bathymetry and sediment thickness data. GIE intensity distributions are computed for external geomagnetic variations at periods of 200, 800 and 3,600 sec. The GIE intensity is normalized with respect to the magnetic variation of 100 nT at Kakioka Magnetic Observatory. The GIE appears significantly enhanced mainly in coastal areas. In addition, the enhancement penetrates a few tens of kilometers inland. From the present calculations, we identify the areas where the GIEs can be largely enhanced, these are (1) the northeast coast along the Sea of Okhotsk, in Hokkaido; (2) the west coast along the Sea of Japan, in southern Hokkaido and Aomori Prefecture (Matsumae-Tsugaru area); (3) the northwest coast along the Sea of Japan, in Niigata Prefecture and Toyama Bay; (4) the southwest coast of the Pacific Ocean; and (5) the east coast of the Korean Peninsula. Further we need to know the geomagnetically induced currents (GICs) in Japan. However, we cannot calculate the GICs in Japan because the power line parameters are not disclosed by policy of Japanese power line companies.

## 1. Introduction

The solar flares sometimes result in severe geomagnetic disturbances called by the magnetic storms. The storms are characterized by the geomagnetic variations with the amplitudes as large as several 1,000 nT in the high-latitudes and several 100 nT in middle- and low-latitudes like Japan. The storm-time magnetic disturbances in the middle- and low-lat-

itudes tend to have large depression in the north-south component. These geomagnetic disturbances are caused by the westward current in the magnetosphere (the equatorial ring current). The current understandings of the magnetic storm are referred to Kamide et al (1997) and references therein.

The magnetic storms induce an electric field in the Earth. Then a potential difference between two

neutral points of transformers in an electrical power line system. That causes the geomagnetically induced currents (GICs). They sometimes damage electrical power line systems in high-latitude countries [Kapfenman, 2005]. For example, a severe GIC resulted in a wide-area blackout in 1989 in Canada [Bolduc, 2002]. Thus, many investigations have studied GICs in high-latitude countries [Pulkkinen et al., 2008], but few have examined GICs in middle-latitude countries [Gaunt and Coetzee, 2007; Torta et al., 2012].

Japan is among the low-latitude countries where GICs have been rarely investigated. The unique report is the GIC intensity measurement at a transformer station in central Hokkaido (the northern part of Japan) [Watari et al., 2009]. It was as small as several Amperes during a moderate geomagnetic storm. This value is negligibly small compared with the permissible current intensity of a typical transformer. It is reported that GICs larger than 100 A sometimes cause transformer accidents in the foreign countries [Tsuboi and Horiuchi, 1988]. In fact, there have been no reports of serious GIC-induced power line failures to date in Japan.

A few recent works have investigated the potential effects of an extreme geomagnetic disturbance [Pulkkinen et al., 2012; Baker et al., 2013]. Such an event does not happen frequently, but could cause serious damage in developed areas (e.g., widespread blackouts). Furthermore, an extreme event could affect not only high-latitude countries, but also middle- and low-latitude regions. For example, the huge magnetic storm in 1859 induced the geomagnetic variation larger than 1,600 nT at Bombay in India [Tsurutani et al., 2003]. (This storm is the biggest one among those recorded scientifically in the history of the geomagnetism research. The intensity of this storm is roughly 3-times larger than the 1989 storm [Tsurutani et al., 2003].) After the 2011 Tohoku-oki Earthquake, which was the highest-intensity earthquake in Japan in the past 1,000 years, the Japanese government is aware of the importance of preparing for such a rare but serious event. It should be noted that Ministry of Economy, Trade, and Industry announced importance of the basic research of GICs in Japan [METI, 2015]. From this viewpoint, we should not ignore the potential danger of GIC disasters, even in low-latitude countries like Japan. Although the results of GIC observation in Hokkaido

[Watari et al., 2009] seem to indicate that Japan is safe from GIC disasters, we cannot simply generalize their findings to any GIC accident, because we do not know the theoretical maximum intensity of an extremely severe GIC. For this reason, it is important to evaluate the potential effects of an extremely severe GIC in Japan.

Three matters must be investigated simultaneously in order to gauge the social effects of an extremely severe GIC. First, the intensity and occurrence rate of extreme severe space weather must be evaluated (the space science). Second, intensity of the geomagnetically induced electric fields (GIEs) must be calculated based on a realistic ground resistivity structure (the geomagnetism). Third, GICs due to such extreme disturbances must be quantitatively evaluated by using the circuit parameters of power line systems are known (e.g., impedances of transmission lines, contact resistances of transformers) [Pirjola, 2008]. Thus, the GIC research is interdisciplinary.

Responding to the needs raised by [METI, 2015], we need to investigate basic information about the GICs. For instance, we do not have a nationwide intensity map of the GIE at the surface of the Earth. The GIE is known to be very sensitive to a local electrical resistivity distribution. (Rough estimation of GIE in Japan by the electrical engineering paper assumed uniform resistivity [Tsuboi and Horiuchi, 1988]. This treatment is not justified in Japan.) Therefore, the heterogeneous resistivity structures of the ground in Japan whose horizontal scales are comparable to the vertical skin depth (about 10 km for typical storm-time variations in the ground with resistivity of 10  $\Omega$ m) should be reflected in the estimation of the GIE. It is also important to identify areas where the GIE intensity is enhanced in Japan for fundamental investigation of the GIC issues in Japan. We therefore focus on estimating the GIE in this paper before estimating the GICs.

Previous modeling studies of the GIE have generally assumed a horizontally uniform ground resistivity [Pulkkinen et al., 2010]. However, studies on the structures of the inside of the Earth have revealed that ground resistivity is significantly heterogeneous, both horizontally and vertically [Ferguson et al., 2012]. These studies also found that the GIE is enhanced at a resistivity boundary, because electric

current is continuous across the boundary. Therefore, anomalously large GIEs are observed in boundaries between conductive sea and resistive land (the “coast effect”) [Parkinson, 1962]. Therefore, it is appropriate that evaluations of GIE heterogeneity have been performed in the U.K. [Beamish et al., 2002; McKay, 2004]. Coastal resistivity contrasts substantially affect GIE estimates in the global-scale modeling [Pütke and Kuvshinov, 2013].

Because Japan is an island country, the GIE in Japan might also be strongly influenced by the coast effect. Geomagnetic transfer functions in Japan are strongly affected by resistivity contrasts in coastal areas [Fujiwara and Toh, 1996]. This fact means that electromagnetic induction patterns in Japan are predominantly influenced by resistivity heterogeneities. In addition, GIE observations in Hokkaido, Japan were made with a network of telecommunication cables a few tens to a hundred kilometers long [Uyeshima et al., 2001]. Because their GIE distribution was resolved on spatial scales as small as several tens of km, they concluded that the spatial features of GIEs in Hokkaido were roughly reproduced using the regional distributions of sea and land.

As ground resistivity structure could significantly affect estimates of the GIE and GIC in Japan, GIC models from Hokkaido alone [Watari et al., 2009] do not generalize directly to the entire country. Thus, it is crucial to investigate GICs in other areas of Japan. For this purpose, it is important to characterize the GIEs using a three-dimensional model of ground resistivity in an appropriate scale.

The GIE in Japan is modelled by using a realistic geomagnetic storm as the induction source, and a near-surface 3D resistivity structure estimated from bathymetry and sediment thickness data [Pütke et al., 2014]. This research found that GIEs in the coastal region significantly exceeded estimates obtained from 1-D resistivity models. However, the  $1^\circ \times 1^\circ$  mesh size was too coarse to discuss the power-line-scale spatial heterogeneities that might affect the GIE in Japan. This partly motivates the present study. In this work, we employ a finer mesh and a heterogeneous ground resistivity model to calculate the GIE intensity map in Japan.

The remainder of this paper is organized as follows. The next section consists of three sub-sections that explain the numerical modeling technique

used in this work. The first sub-section describes the numerical technique itself, the second covers the construction of the mesh system, and the third deals with the ground resistivity structure. The third major section describes our numerical results, with a focus on local characteristics of GIE intensity. The fourth section describes further efforts to characterize GIE in detail. The last section summarizes the main results.

## 2. Method

### 2.1 Theory

In order to resolve the spatial distribution of the GIEs in and around Japan, we use the global electromagnetic induction code of Uyeshima and Schultz (2000), with a staggered mesh scheme for finite-difference calculation of the electric and magnetic fields. The magnetic and electric fields are given at the corner point of a mesh and at the center of the mesh, respectively, as shown in Fig. 1 of Uyeshima and Schultz (2000). Given an inductive source external to the Earth (this region is henceforth simply referred to as “the air”), this code solves for the electromagnetic induction of a spherical Earth in the frequency domain. We use the global code to calculate regional induction in order to avoid the difficulties caused by horizontal boundaries. We note that this method ignores magnetospheric plasmas.

To obtain the practical GIE intensity map, it is important to model the magnetospheric source current in detail. On the other hand, it is sufficient to employ one element of the source current for fundamental studies of the GIE intensity map itself. Each element has a specific frequency, spatial variations denoted by a unique spherical harmonic, and a normalized intensity. The latter approach is naturally expanded to the former because any geomagnetic field variation can be represented by linear combinations of GIEs from the elementary source current. Therefore, we model induction due to a simple external source in the frequency domain; we calculate the electromagnetic response of the ground based on periodic external magnetic variations as a function of frequency.

We now briefly review how to calculate ground induction via numerical modeling. Let the Fourier amplitudes of magnetic field variation and the electric current variation be denoted  $\tilde{\mathbf{B}}$  and  $\tilde{\mathbf{J}}$ , respectively (the

Fourier amplitude of each parameter is denoted by the tilde.) The electromagnetic response of the external source current ( $\mathbf{J}_{\text{ext}}$ ) is expressed by the equation,

$$\nabla \times \tilde{\mathbf{B}}(\mathbf{r}, \omega) = \mu_0 \tilde{\mathbf{J}}(\mathbf{r}, \omega) + \mu_0 \tilde{\mathbf{J}}_{\text{ext}}(\mathbf{r}, \omega), \quad (1)$$

where  $\mathbf{r}$  and  $\mu_0$  are the position and magnetic permeability of a vacuum, respectively. We assume no additional permeability from other materials.

The source current,  $\mathbf{J}_{\text{ext}}$ , is given at 10 Earth radii (63,710 km) as a boundary condition. It flows circularly on the equatorial plane, with the flow direction changing as a function of angular frequency,  $\omega$ . This source current then induces the north-south source magnetic field over Japan region. Note that we choose this source current as an arbitrarily example of a large-scale simple source. This is eventually similar to the equatorial ring current of the magnetic storm, but we do not intend to simulate the GIEs in the magnetic storm. To model magnetic sources with arbitrary polarizations, the plane of the source current flow is assigned an arbitrary inclination  $\alpha$  with respect to the equatorial plane. The inclined plane intersects the equatorial plane at 137.5°E and 42.5°W with inclination angle  $\alpha$ : the sense of  $\alpha$  is positive when current is inclined anticlockwise from east to west.

The induced current  $\tilde{\mathbf{J}}$  in Eq. (1) yields an electric field ( $\tilde{\mathbf{E}}$ ) in the resistive medium, with electrical resistivity  $\rho$ . Thus, we have

$$\tilde{\mathbf{E}}(\mathbf{r}, \omega) = \rho(\mathbf{r}) \tilde{\mathbf{J}}(\mathbf{r}, \omega). \quad (2)$$

Angular frequencies of storm-time magnetic variations are so low that we can neglect polarization current [Püthe et al., 2014]. In our modeling,  $\rho$  is assumed to be a scalar.

The induction equation,

$$\nabla \times \tilde{\mathbf{E}}(\mathbf{r}, \omega) = i\omega \tilde{\mathbf{B}}(\mathbf{r}, \omega), \quad (3)$$

describes the relationship between the electric and magnetic fields. Here,  $\tilde{\mathbf{E}}$  and  $\tilde{\mathbf{B}}$  are numerically calculated from given values of  $\rho$  and  $\tilde{\mathbf{J}}_{\text{ext}}$ . A more detailed description of the numerical technique can be found in Uyeshima and Schultz (2000).

## 2.2 Mesh system

We employ a biased mesh system with finer meshes in Japan and surrounding areas. The horizontal mesh size is 0.125° over 25-50°N and 125-150°E in order to reproduce the realistic resistivity structure in Japan; these are much finer than the 1° × 1° mesh employed by Püthe et al. (2014). The mesh size outside Japan is gradually widened to 5°.

In the vertical direction, a finer mesh spacing is used near the Earth's surface ( $r = 6371$  km denoted with a broken line). The finest mesh spacing is 1.0 km around the Earth's surface, and mesh width increases with increasing distance from the surface of the Earth. For instance, the second to fifth meshes have widths of 1.5, 2.5, 2.5, and 5.0 km, respectively. (So, the mesh positions from the surface are 1 km, 2.5 km, 5 km, 7.5 km, 12.5 km.) This mesh structure guarantees that numerical results near the surface have the highest accuracy of any values in the model, because these mesh widths are sufficiently smaller than the skin depths of the most conductive material (seawater) in this study at the periods considered. For example, the skin depth of the 100 sec variation is  $\sim 10$  km in seawater with resistivity 0.33  $\Omega\text{m}$ .

The upper and lower altitude boundaries for these calculations are 63,710 km (10 times of Earth's radius) and 3,479 km, respectively. Both boundaries are far enough so that electric and magnetic variations near the Earth's surface do not reach these boundaries. The resistivity below the lower boundary (the mantle-outer core boundary) is set to zero to ensure no induction beyond the boundary.

The mesh is divided into 189 total meshes in longitude, 153 total meshes in latitude, and 81 total meshes in altitude.

## 2.3 Resistivity model

In order to calculate local to the regional GIEs in Japan, we need to consider the distribution of ground resistivity in three dimensions. Some 3-D regional models of the ground resistivity distribution in Japan have been reported recently, based on direct measurements [Kanda and Ogawa, 2014; Hata et al., 2015]. However, measurements are not yet available for the entire region. Therefore, it is necessary to use an inferred model for ground resistivity.

In the present paper, we utilize land topography and bathymetry data from ETOPO1 [Amante

and Eakins, 2009], along with a global digital map of sediment thickness [Laske and Masters, 1997], to estimate ground resistivity in the near-surface area. Using these two data sets, the near-surface area can be divided into a seawater region, a sedimentary region, and a rock region. We generate a 3-D near-surface resistivity distribution by assigning typical resistivity values to each region. Radially symmetric (1-D) layers are used underneath the heterogeneous near-surface layers.

This resistivity model mainly features a large resistivity contrast between sea water (0.2-0.5  $\Omega\text{m}$ ) and rock (typically, 100 to 10,000  $\Omega\text{m}$  for the crust). Inclusion of the sediment region gives better accuracy to the resistivity model. The sea-land contrast is the most severe and has the relevant spatial scale for the GIE of the power line in Japan. The crustal rock can have a resistivity as small as 0.1-1  $\Omega\text{m}$ , however those extreme values are ‘anomalies’ and would not last in the powerline scale.

It is noted that bathymetry data have a resolution of  $1' \times 1'$ , but sediment data have a resolution of  $1^\circ \times 1^\circ$ . It is important to utilize a horizontal mesh size as small as several tens of kilometers to calculate GIEs in Japan, due to the region’s complex geography. Thus, to match the spatial resolution of the sediment data to that of the bathymetry data, we use the bicubic interpolation method of the General Mapping Tools software package [Wessel and Smith, 1998]. Fig. 1 shows the bathymetry–altitude map in the left panel, and the interpolated sediment thickness map in the right panel.

Here, we explain how we determine resistivity

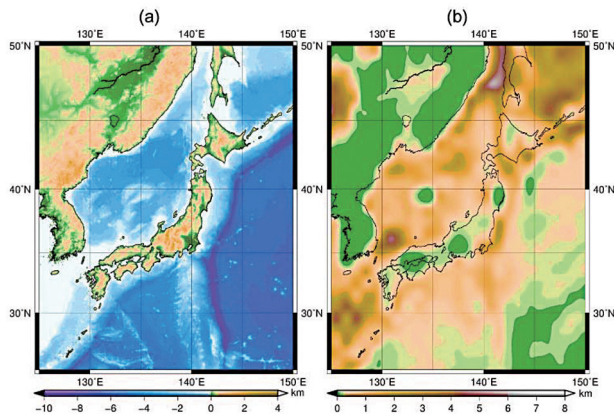


Fig. 1 (a) Bathymetry and altitude, and (b) sediment thickness, in and around Japan. Sediment thickness is interpolated to a  $1' \times 1'$  mesh.

on the computational mesh. In our staggered mesh system, resistivity is given at the center of a mesh reflecting the portion of sea water, sediment and rock in it.

Let bathymetry and sediment thicknesses at  $\theta$  (co-latitude) and  $\Psi$  (longitude) be  $z_b(\theta, \Psi)$  and  $z_s(\theta, \Psi)$ , respectively.  $\theta$  and  $\Psi$  locate the center of the top surface of a mesh which represents the uppermost ground (Fig. 2). Altitude is neglected in this study; i.e.,  $z_b(\theta, \Psi) = 0$  on land. The bathymetry and sediment thickness data are given on finer meshes than our computational mesh at the surface of the Earth. Thus, some surface computational meshes have multiple bathymetry and sediment thickness values. To compensate, we arrange the data onto the horizontal computation mesh by averaging values included in each mesh.

For the sea region, let  $z_b(\theta, \Psi)$  denote the depth of the seawater. We set  $z_b(\theta, \Psi)$  equal to the depth of the top of the sediment; thus,  $z_b(\theta, \Psi) + z_s(\theta, \Psi)$  gives the depth of the top of the crustal rock. Therefore, the boundaries between seawater and sediment, as well as between sediment and rock, are determined on the computational mesh. We then assign each mesh to the portions of seawater, sediment, and rock included in that mesh. Let  $d_w(\theta, \Psi, r)$ ,  $d_s(\theta, \Psi, r)$  and  $d_r(\theta, \Psi, r)$  denote the widths of seawater, sediment and rock, respectively, for the mesh centered on  $\theta, \Psi$  and  $r$ . When the mesh is occupied by one or two regions, the width(s) of excluded region(s) is zero. The

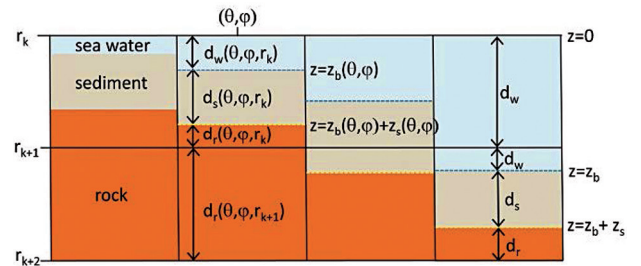


Fig. 2 Schematic view of the computational mesh and distributions of seawater, sediment and rock.  $r_k$  means the  $k$ -th node in the  $r$  direction. The depths of sea water and sediment  $z_b(\theta, \Psi)$  and  $z_s(\theta, \Psi)$  are given at the center of the top surface of the uppermost mesh for the ground  $\theta$ (co-latitude) and  $\Psi$ (longitude). The widths of seawater, sediment and rock,  $d_w(\theta, \Psi, r)$ ,  $d_s(\theta, \Psi, r)$  and  $d_r(\theta, \Psi, r)$ , respectively, are computed from  $z_b(\theta, \Psi)$  and  $z_s(\theta, \Psi)$  for each subsurface mesh.

conductivity  $\sigma(\theta, \Psi, r)$  of the mesh is the average of the conductivities of the three regions, weighted by the relative proportions of each:

$$\sigma(\theta, \varphi, r) = \frac{d_w(\theta, \varphi, r)}{d(r)} \frac{1}{\rho_w} + \frac{d_s(\theta, \varphi, r)}{d(r)} \frac{1}{\rho_s} + \frac{d_r(\theta, \varphi, r)}{d(r)} \frac{1}{\rho_r}, \quad (4)$$

where  $\rho_w$ ,  $\rho_s$ , and  $\rho_r$  denote the resistivities of seawater, sediment, and rock, respectively.  $d$  is the width of the mesh. In this work we assume  $\rho_w = 0.33 \Omega\text{m}$ ,  $\rho_s = 10 \Omega\text{m}$ , and  $\rho_r = 1,000 \Omega\text{m}$ , respectively. The resistivity,  $\rho(\theta, \Psi, r)$ , is simply the reciprocal of conductivity; i.e.,  $\rho(\theta, \Psi, r) = 1/\sigma(\theta, \Psi, r)$ .

Fig. 3 shows the resistivity distribution of the uppermost mesh of the ground (1 km width) in and around Japan. It is evident from Figs. 2 and 4 that lower-resistivity areas in the deep sea invoke striking contrasts with higher resistivity areas on land. It is noted that these contrasts are reproduced by the present the  $1' \times 1'$  mesh calculation. We also notice comparatively low-resistivity patches that reflect geological structures on land and in the shallow-water region. For example, depressed resistivity appears in the Kanto Plain and in Akita Prefecture of Honshu, as well as the Ishikari and Tokachi plains of Hokkaido;

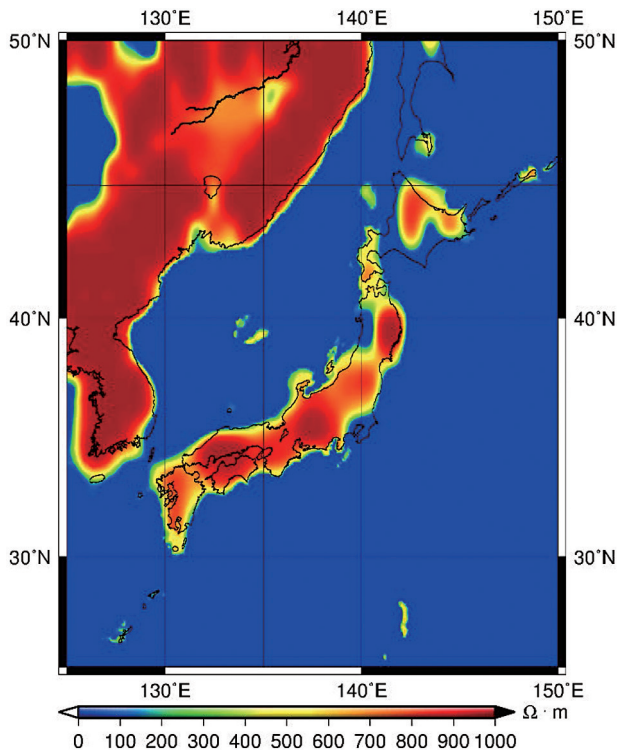


Fig. 3 Resistivity distribution from the surface to 1 km.

these low-resistivity areas are associated with thick sediment. The low-resistivity area in Akita Prefecture is also seen in the 3-D resistivity model of Kanda and Ogawa (2014). It is expected that these low-resistivity areas act like shallow sea areas in terms of electromagnetic induction.

Fujiwara and Toh (1996) and Uyeshima et al. (2001) performed thin sheet modeling with resistivity models that consisted of seawater and rock. Since we include sediment, our resistivity model shows spatially smooth variations. Such a fine-scale ground resistivity structure is important in evaluating GIEs.

The rock region extends to a depth of 42 km. The region beyond this depth is the upper mantle, with  $500 \Omega\text{m}$  resistivity and a thickness of 758 km; i.e., extending from 42 km to 800 km below the surface. The lower mantle, with resistivity  $0.5 \Omega\text{m}$ , has a thickness of 2,092 km (extending from 800 km to 2,892 km below the surface). The outer core, at  $r < 3,479$  km (extending from 2,892 km below the surface), is assumed to be a perfect conductor. It is noted that these deeper parts of the Earth do not significantly affect induction for the geomagnetic variations concerned.

### 3. Results

#### 3.1 GIE induced by north-south magnetic variation

We now show numerical estimates of GIE intensity in and around Japan. The GIEs induced by external magnetic variations with periods of 200, 800, and 3,600 sec are discussed in the present report. The 200 sec variations roughly correspond to the time scale of the geomagnetic sudden commencement which is invoked by sudden compression of the magnetosphere due to the solar wind shock [Araki, 1997]. The 3,600 sec variations represent the magnetic sub-storm associated the severe auroral activity in the polar region [Akasofu, 1964]. First, we show GIE intensity for external magnetic variations polarized in the north-south direction (i.e., the source current flowing in the equatorial plane). Subsequently, we discuss GIE intensity caused by external magnetic variations, with horizontal vectors declined from north (i.e., the source current inclined from the equatorial plane).

Fig. 4 shows the GIE intensity map in and around Japan at a period of 200 sec, when the source current induces north-south magnetic variations on

the ground. GIE intensities shown in this figure are normalized with respect to a geomagnetic intensity at Kakioka of 100 nT. Hereafter, all GIE intensity maps use the same normalization. Fig. 4 also shows that GIE intensity varies locally across Japan; the GIE is uniform and very small in the ocean, whereas patchy patterns are resolved on land. The GIE amplitude on land ranges from about 500 to 2500 mV/km. These variations reflect the heterogeneous distribution of ground resistivities in Fig. 3.

The GIC and GIE have been previously estimated under the assumption of a horizontally homogeneous surface resistivity [Pulkkinen et al., 2010]. Thus, it is interesting to compare the GIE in the heterogeneous resistivity case (i.e., Fig. 4) with that of the homogeneous resistivity case. This comparison will emphasize the coast effect. Fig. 5 shows the ratio of GIE estimated from a heterogeneous model (Fig. 4) to that estimated from a homogeneous model with uniform (1,000  $\Omega\text{m}$ ) surface layers. We use the same

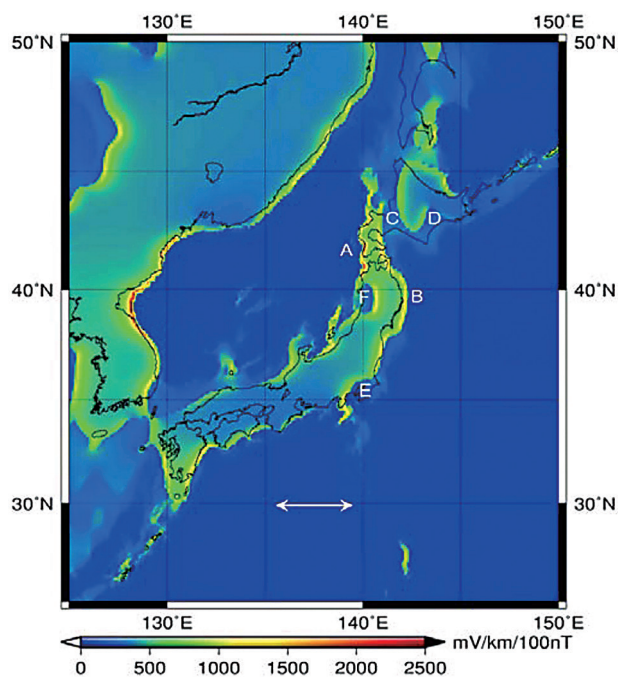


Fig. 4 GIE intensity in and around Japan for the equatorial source current at a 200 sec period. GIE intensity is normalized to match the 100 nT magnetic intensity at Kakioka. The white arrow indicates the direction of the source current. The GIE is enhanced along the west coast of Matsumae Peninsula and Tsugaru Peninsula (A), and along the east coast of Iwate Prefecture (B). The GIE is depressed in Ishikari Plain (C), Tokachi Plain (D), in Kanto Plain (E), and Akita Prefecture (F).

equatorially flowing (east–west) source current for both cases. This figure clearly shows that the GIEs are enhanced when coastlines trend north–south. These coastlines are perpendicular to the direction of the source current, which is perpendicular to the direction of the primary current induced in a uniform medium. This GIE enhancement penetrates a few hundred kilometers onto land, especially when the land is narrow or resistive (i.e., shallow sediment). Peaks of enhanced-GIE regions have widths as narrow as a few tens of kilometers.

We notice intensified GIEs (as large as 2500 mV/km, for the 100 nT magnetic variation at Kakioka) along the west coast of Matsumae Peninsula, Hokkaido, and on the west coast of Tsugaru Peninsula (labeled “A” in Fig. 4). The GIE is also enhanced on the conjugate coastlines of Iwate Prefecture, on the Pacific Ocean (labeled “B” in Fig. 4), but the in-

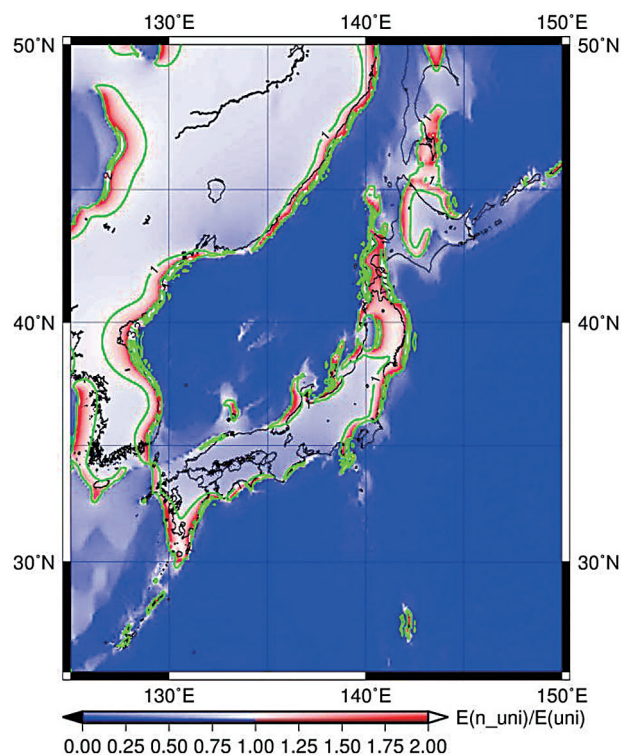


Fig. 5 Ratio of GIE modeled with a heterogeneous surface to GIE modeled with a homogeneous surface. A source current is placed on the equatorial plane and oscillated with a 200 sec period. Absolute values of the complex ratio are shown. Areas where the heterogeneous GIE is larger/smaller are shaded red/blue, respectively. Green solid curves are isolines corresponding to a ratio of unity. Heterogeneous areas reflect the land-sea distribution and sediment thickness in the area, while homogeneous areas are made of rock. Rock resistivity is fixed at 1,000  $\Omega\text{m}$ .

tensity is smaller than that of the Matsumae-Tsugaru region. This asymmetry comes from differences in the resistivity structures of each region's respective coastal areas. In the Matsumae-Tsugaru region, the deep sea is close to the coast, whereas this is not the case for Iwate Prefecture (Fig. 1a). The concentration of GIEs due to the deep sea's proximity can be seen in a cross-section of GIE and electric current distributions in Matsumae Peninsula (Fig. 6). Fig. 6 illustrates the electric current vectors in an arbitrary scale at  $t=0$  in the cross section. (As the current is expressed as  $\tilde{J}(\mathbf{r}, \omega)e^{i\omega t}$ , the current at  $t=0$  is the real part of  $J$ .) The sea depth is  $\sim 1$  km next to the coastal mesh in the peninsula. The electric current has a large vertical component just offshore, which converges in the horizontal direction at the coastal mesh. Although the electric current has no vertical component at the surface (air has almost infinite resistivity), the vertical component can propagate to subsurface layers. Thus, due to the resistivity distribution, the induced electric current is distributed three-dimensionally in Matsumae Peninsula, giving a wide range of GIE values at the surface. It is noted that the mountains above the sea level do not affect significantly the GIE distribution because currents induced in the mountains can flow along the ground.

It is evident from Fig. 4 that reduced surface GIEs appear in the Ishikari Plain ("C" in the figure) and Tokachi Plain ("D") regions of Hokkaido, and in Kanto Plain ("E") and in Akita Prefecture ("F") of Honshu. All of these regions are characterized by

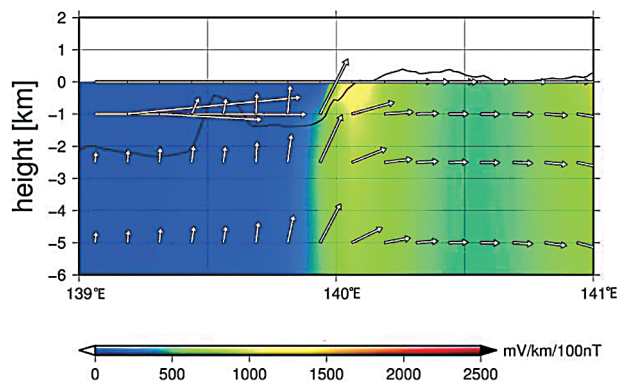


Fig. 6 Cross-section of GIE intensity (color contours) and electric current (white arrows) in Tsugaru Peninsula at  $t=0$ . The current vectors are shown in an arbitrary scale. Cross-section latitude is  $41.875^\circ\text{N}$ . Bathymetry and altimetry are indicated by black lines. Altimetry above sea level is ignored in this study.

low resistivities due to great sediment thicknesses (Fig. 1b). Slightly enhanced GIEs appear at the rims of these low-GIE regions, caused by the resistivity contrast between sediment and rock. This feature was already reported that an enhanced GIE should be seen at the margin of the Kanto Plain, because the sediment-basement rock boundary causes a weak coast-like effect [Honkura, 1985]. We also note that a strongly enhanced GIE is observed along the east coast of the Korean Peninsula.

Fig. 7 shows the GIE intensities for external magnetic variations with periods of 800 sec and 3,600 sec, assuming external magnetic variations are oriented north-south. Naturally, the net GIE intensity is reduced (relative to that of 200 sec variations), which follows directly from Faraday's law. However, the general spatial pattern of enhanced GIE intensities in coastal areas does not change. Thus, the GIEs responsible for GICs on power line systems are substantially affected by near-surface resistivity structure in and around Japan, for magnetic variations with time scales of 200-3,600 sec. These are typical time scales for external geomagnetic disturbances. Spatial variations in GIC intensity will be strongly affected by sharp changes in surface resistivity along the routes of power lines.

### 3.2 GIEs from various source polarizations

Since geomagnetic disturbances in the magnetosphere are not only polarized in the north-south direction, we need to investigate the dependence of GIE intensity on polarization direction. In this analy-

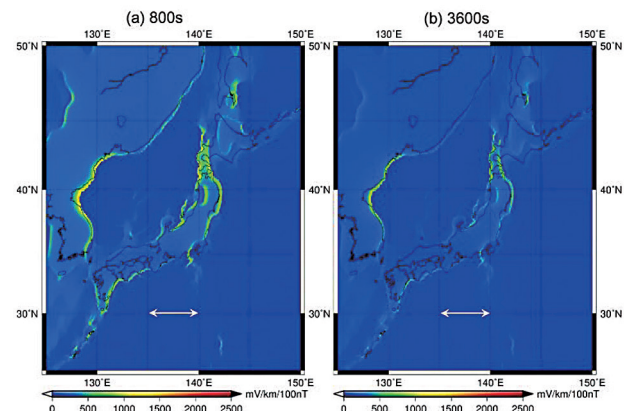


Fig. 7 GIE intensity in and around Japan for external current with (a) 800 sec period and (b) 3,600 sec period. The source current is placed on the equatorial plane.

sis, the source current at 63,710 km is inclined relative to the equatorial plane, so that induced magnetic variations in the Japan region have arbitrarily polarized directions with inclination angle  $\alpha$ . Fig. 8 shows GIE intensity plots for  $\alpha = -30^\circ$  and  $60^\circ$ . When these results are compared with Fig. 4, we notice that the GIE is enhanced in different locations. For example, with  $\alpha = 60^\circ$  the GIE is greater in the western half of Honshu than in the eastern half; this is the opposite of the pattern in Fig. 4. For  $\alpha = -30^\circ$ , the GIE is generally large in most of the Japanese islands. In both cases, an enhanced GIE appears along the Pacific coast of southwest Japan ("A" in Fig. 8). These differences may arise because the induced electric current

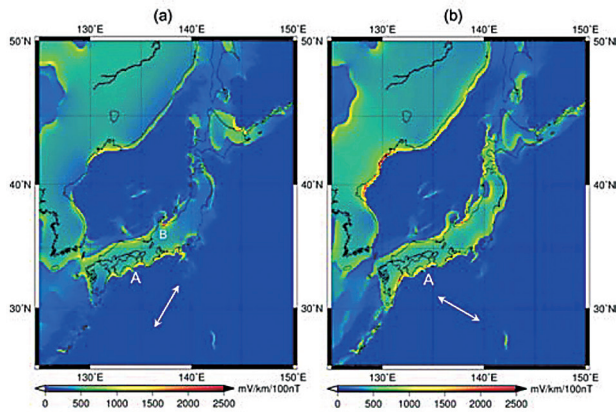


Fig. 8 GIE intensity distributions in and around Japan for inclined source currents with a period of 200s. Source current is inclined (a)  $60^\circ$  and (b)  $-30^\circ$  relative to the equatorial plane.

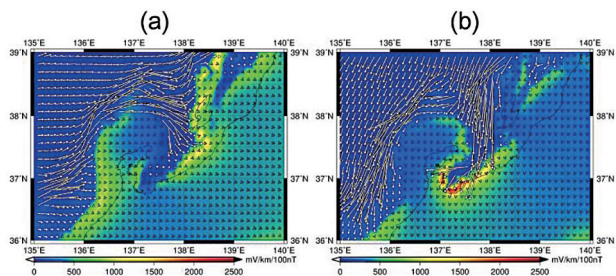


Fig. 9 GIE intensity and electric current at Toyama Bay for inclined source currents. GIE intensity (color contours) and electric current (white arrows) are computed at a period of 200 sec. The source current is inclined (a)  $0^\circ$  and (b)  $60^\circ$  with respect to the equatorial plane. Snap shots when the GIE and current amplitudes are near their maximum values are shown: (a)  $t=150$  sec and (b)  $t=50$  sec. The electric current vectors in each figure are shown in an arbitrary scale.

in the ocean has a component perpendicular to the coast when the inducing magnetic field has a component parallel to it.

The GIE shows a sharp peak at the coast of Toyama Bay ("B" in Fig. 8a). Toyama Bay is the terminus of a deep, narrow bay structure formed by Honshu and Noto Peninsula. This geography results in a conductive narrow path along the coast, and a sharp resistivity boundary at the coast of Toyama Bay (Fig. 4). When the source electric current flows parallel to the axis of the bay structure ( $\alpha = 60^\circ$ ), the induced electric current in the ocean is concentrated in the narrow conductive path, and reaches Toyama Bay (Fig. 9b). The same mechanism seen in Fig. 6 enhances the GIE at the coast of Toyama Bay. If the source electric current is not parallel to the axis of the bay structure, then intensification of the electric current and GIE is only moderate (Fig. 9a). A similar resistivity structure to that of Toyama Bay is seen at Suruga Bay in Fig. 3; therefore, there may be enhanced GIEs at the coast of Suruga Bay when the source electric current flows parallel to the bay axis.

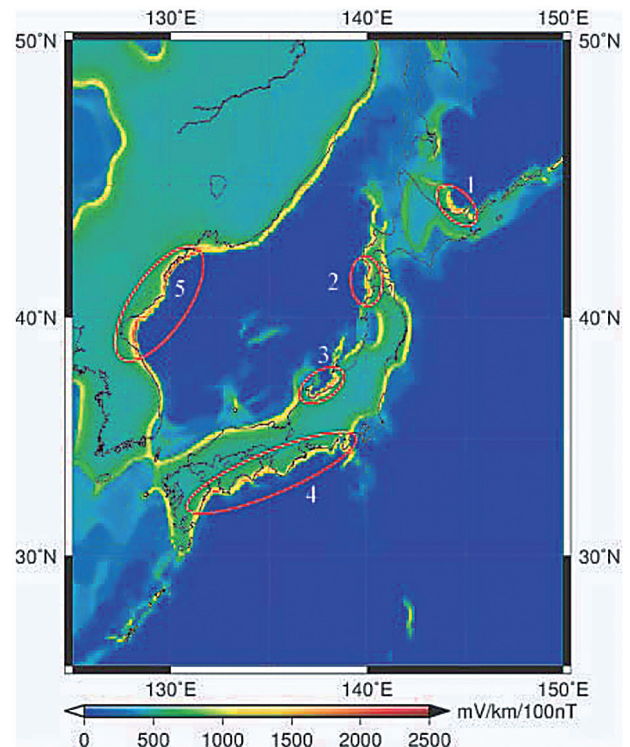


Fig. 10 Maximum GIEs in and around Japan for an external current with an oscillation period of 200 sec. The maximum GIE at each site is taken from five inclination angles ( $-60^\circ$ ,  $-30^\circ$ ,  $0^\circ$ ,  $30^\circ$ , and  $60^\circ$ ). Areas of enhanced GIE intensity tagged with 1~5 are explained in the text.

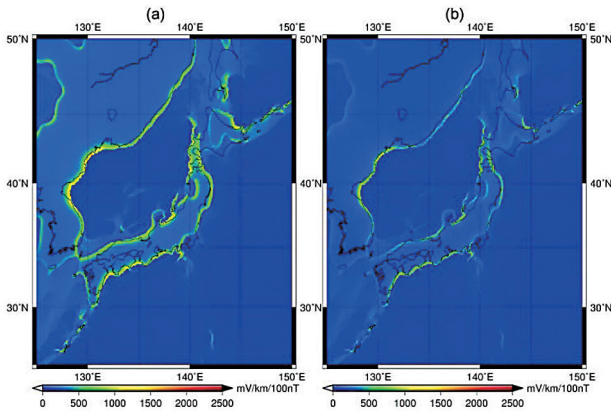


Fig. 11 Maximum GIE maps in and around Japan for external currents with periods of (a) 800 sec and (b) 3,600 sec.

As noted above, GIE intensity depends on the horizontal polarization of the external magnetic field. Thus, GIE intensity reaches its maximum at sites where declination changes continuously. The superposed envelope of the maximum GIEs of all sites yields a map showing theoretical maximum GIE intensity in and around Japan (e.g., Fig. 10). These values can be obtained by changing the inclination angle of the source current. Fig. 10 shows the maximum GIE map for the 200 sec magnetic variation for inclination angles of  $\alpha = 60^\circ, 30^\circ, 0^\circ, 30^\circ,$  and  $60^\circ$ . This figure indicates five areas of intensified GIE: (1) the northeast coast along the Sea of Okhotsk, in Hokkaido; (2) the west coast along the Sea of Japan, in southern Hokkaido and Aomori Prefecture (Matsushima-Tsugaru area); (3) the northwest coast along the Sea of Japan, in Niigata Prefecture and Toyama Bay; (4) the southwest coast of the Pacific Ocean; and (5) the east coast of the Korean Peninsula. An intensified GIE appears in the same areas for 800 sec and 3,600 sec GIEs (Fig. 11).

## 4. Discussions

### 4.1 Resistivity in the rock region

We estimated GIE intensity using heterogeneous near-surface resistivity, with typical values of resistivity for seawater, sediment, and rock. The resistivities of seawater and sediment are appropriately typical values, because seawater resistivity ranges from 0.25 to 0.5  $\Omega\text{m}$  (depending on temperature and salinity), and sedimentary resistivity ranges from 1 to 50  $\Omega\text{m}$ . On the other hand, the resistivity of crustal rock can vary from  $\sim 0.1$  to 10,000  $\Omega\text{m}$ , and resistivity in the

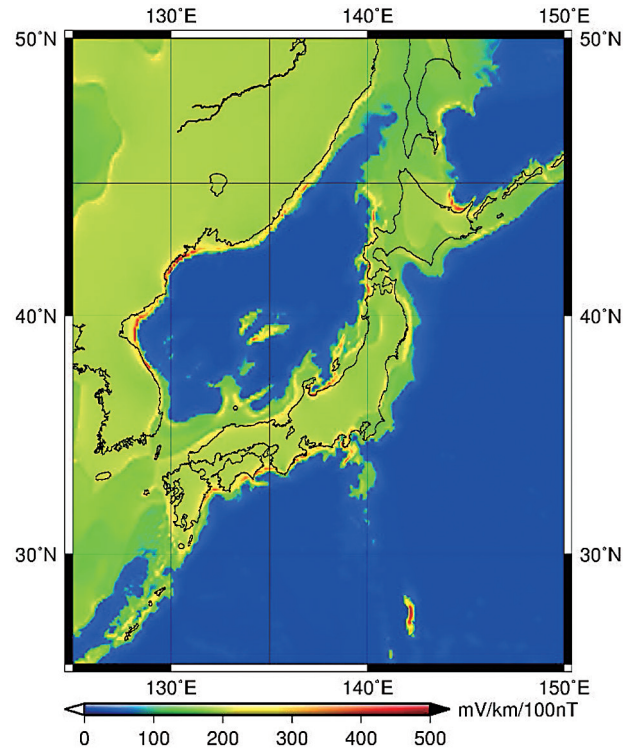


Fig. 12 Maximum GIE maps in and around Japan for a rock resistivity of 100  $\Omega\text{m}$ , with an applied 200 sec current.

upper mantle can vary from 10 to 1,000  $\Omega\text{m}$  [Evans, 2012]. A resistivity value of 1,000  $\Omega\text{m}$  for rock regions above 42 km was chosen in the present study as a representative value for the resistive lithosphere (i.e., crust and brittle upper mantle) in the region. Therefore, we also calculated GIE intensity based on the conductive lithosphere (100  $\Omega\text{m}$ ), to investigate the possible effects of changing resistivity on GIE intensity. Fig. 12 shows the maximum GIEs for a 200 sec current. This figure indicates that rock resistivity significantly affects GIE amplitude in coastal areas. On the other hand, spatial patterns of GIEs are roughly the same as for 1,000  $\Omega\text{m}$ , because the GIE spatial patterns are mainly characterized by enhancement at resistivity boundaries.

### 4.2 Magnetotelluric impedance tensors

As the numerical results described above are not confirmed by real observation, it is important to compare the numerical results with the observed one. However, the direct measurements of the GIEs all over Japan have not been conducted yet. Instead, we treat the magnetotelluric induction vectors which were measured by Uyeshima et al. (2001).

As shown above, the GIE is highly sensitive to

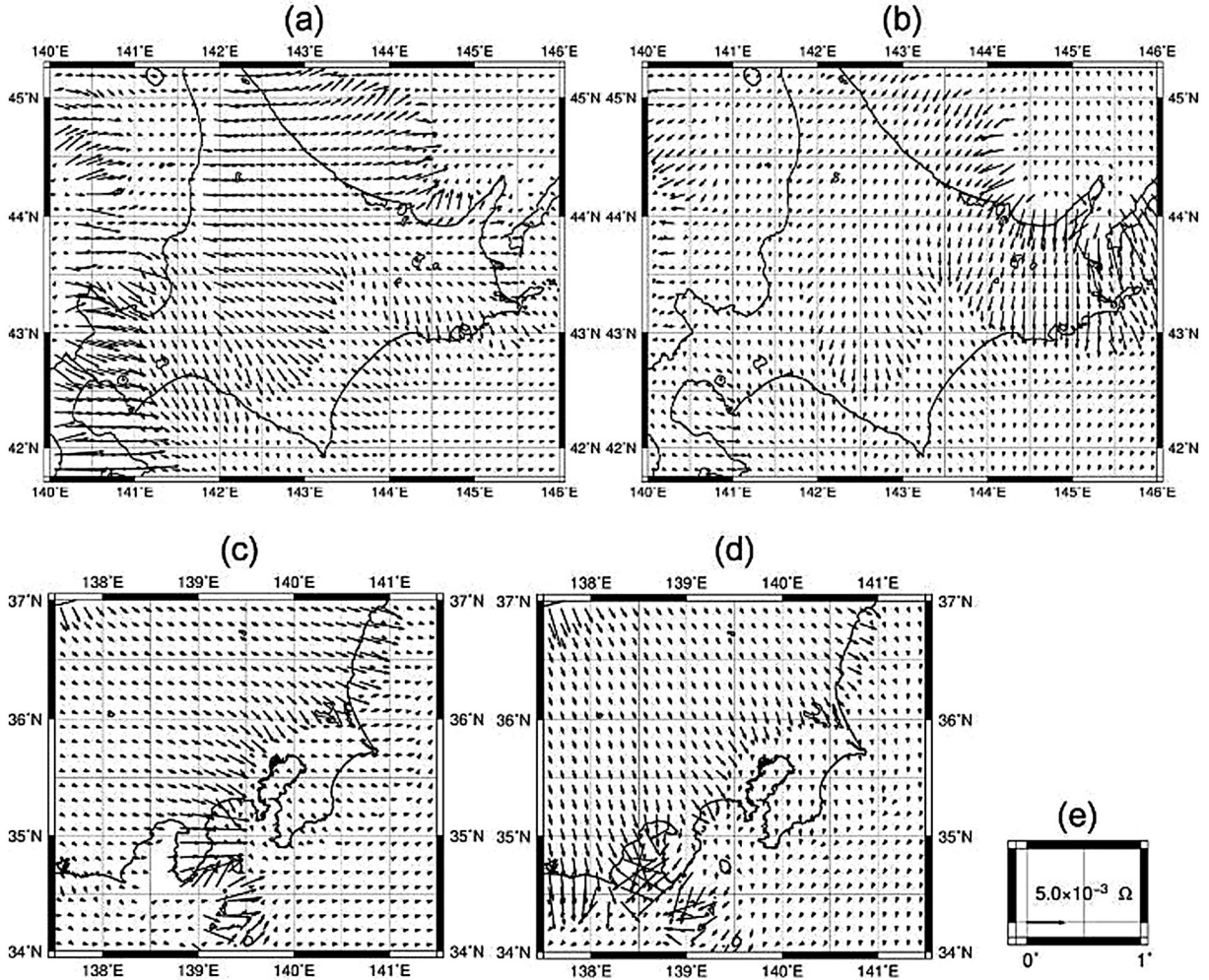


Fig. 13 Magnetotelluric impedances for a 3,600 sec equatorial source current in Hokkaido (a, b) and Kanto (c, d). Vectors of  $\text{Re}(Z_{xx})$  and  $\text{Re}(Z_{yx})$  are shown in (a) and (c), and vectors of  $\text{Re}(Z_{xy})$  and  $\text{Re}(Z_{yy})$  are shown in (b) and (d), respectively. The arrow in (e) denotes a scale reference impedance vector of  $5.0 \times 10^{-3} \Omega$ .

the resistivity distribution of the Earth. Therefore, it exhibits a complicated pattern at the surface. This fact indicates that a 1-D model does not fully reproduce the full complexity of true GIEs in Japan. As often shown in magnetotellurics (hereafter MT) [Cagniard, 1953], the 1-D assumption breaks down when MT impedances are considered. MT impedance,  $Z_{ij}$  ( $i, j = x, y$ ), appears in the following expression,

$$\begin{pmatrix} E_x(\omega) \\ E_y(\omega) \end{pmatrix} = \frac{1}{\mu_0} \begin{pmatrix} Z_{xx}(\omega) & Z_{xy}(\omega) \\ Z_{yx}(\omega) & Z_{yy}(\omega) \end{pmatrix} \begin{pmatrix} B_x(\omega) \\ B_y(\omega) \end{pmatrix}. \quad (5)$$

$Z_{ij}$  ( $i, j = x, y$ ) is also the transfer function of the geoelectric field  $E_i$  to the geomagnetic field  $B_j$ . Fig. 13 shows estimates of MT impedances in the Hokkaido and Kanto Plains at 3,600 sec periods, using our computations of the GIE and magnetic field at the Earth's surface. Fig. 13a and c shows the vector components  $\text{Re}(Z_{xx})$  and  $\text{Re}(Z_{yx})$ , respectively. These

components illustrate how  $B_x$  relates to  $E_x$  and  $E_y$ . Fig. 13b and d shows the corresponding components  $\text{Re}(Z_{xy})$  and  $\text{Re}(Z_{yy})$ , to illustrate how  $B_y$  relates to  $E_x$  and  $E_y$ . These figures clearly show that the magnetic field correlates to the electric field in the parallel direction (i.e., the diagonal component of MT impedance). This reflects the resistivity distribution of the Earth. For instance, in Fig. 13a and b we can recognize the following characteristics of MT impedance at Memambetsu: (1) responses to  $B_y$  have larger amplitudes than responses to  $B_x$ ; and (2) responses to  $B_x$  are relatively 1-D, but responses to  $B_y$  are not. The second feature is consistent with impedances observed by Fujii et al. (2015), and with observations of a strong correlation between the GIC and  $B_y$  near Memambetsu [Watari et al., 2009]. Furthermore, when the impedances in Hokkaido (Fig. 13) are compared with observed values reported by Uyeshima

et al. (2001), their spatial patterns are similar. For example, both the measured and calculated induction vectors are directed toward the coastline in the coast area of the Okhotsk Sea and south-east in the central part of the Hokkaido and in the coast area of Pacific Ocean. Thus, the present calculation is independently validated by existing observations. However, the observed impedances show smaller-scale variations than our computations. This indicates that the observed impedances are influenced by smaller-scale geological structures than present models can consider.

The MT impedance estimates for Kanto Plain (Fig. 13c and d) are a serendipitous consequence of the present study: anthropogenic noise interferes with field measurements of the GIE or geomagnetic field in such highly industrialized, densely populated areas. Yet the same high population density makes it important to estimate GIE in this area. Our numerical results show that the coast effect is seen along the Pacific Ocean, and at the margins of the thick sediment layer. This result is consistent with Honkura (1985). However, their anomalously large  $E_y$  values at Kakioka and patchy distributions of GIEs near Kakioka are not reproduced in Fig. 13. Thus, several key local geological structures might be missed by our model because our model aims at the GIE in the power line scale.

### 4.3 Future issues

We note that the present fine-mesh ( $0.125^\circ \times 0.125^\circ$ ) calculation is capable of reproducing the local GIE enhancement in Japan better than the coarse-mesh ( $1^\circ \times 1^\circ$ ) calculation by Püthe et al. (2014) is. In addition, the local GIE enhancements obtained in this paper are mainly associated with the sharp resistivity contrasts in the sea-land boundary; these contrasts are essentially determined by the bathymetry data. Therefore, the local GIE enhancements in the GIC map seem to be realistic. However, it is noted that the GIE map with much finer mesh configurations may be still desirable in order to confirm convergence of the numerical calculation; this is the future work. In addition, as the 3D resistivity distribution is not confirmed by the measurement of the resistivity. Therefore, the measured resistivity distribution is strongly required for the realistic estimation of the GIEs. Thus, the second future work is to calculate the GIE

map with the measured 3D resistivity distribution in Japan.

The present study manifested the maximum GIE intensity map. The intensity does not refer to the absolute values, but the relative one corresponding to the normalized magnetic variation (100 nT at Kakioka magnetic observatory). To access the absolute value and discuss the possible vulnerability of the transformers in Japanese powerline system, we need information of the magnetic variations of the huge magnetic storm occurring once in 1,000 years. At the same time, it is important to investigate the critical intensity of the GIC that can damage a transformer. However, there is no definite report about the critical GIC. The transformers used in Japan are safe for the GIC of 30 A [Takasu et al., 1993]. On the other hand, there is a report that the GICs more than 100 A may cause damages of transformers in foreign countries [Tsuboi and Horiuchi, 1988]. Recently, it is reported that the Japanese transformers seem to work in safe for the GIC with more than 100 A [METI, 2015] which occurred in Nov. 2003 (the Halloween storm). The intensity of this storm ( $\sim 400$  nT) is about 1/4 of the 1859 storm intensity ( $\sim 1600$  nT). Therefore, the vulnerability of the Japanese transformers is not settled when the huge magnetic storm occurring once in 1,000 years is considered. It is noted that we might predict the huge storm from observations of the sun with a lead time of about 1day.

As a next step, it is important to calculate GICs from the GIE distribution obtained in this paper. To that end, system parameters of the power grid in Japan are required. However, as the information is not disclosed by Japanese electric companies, it is difficult to calculate GICs at the present time.

## 5. Conclusions

After the 2011 East-Japan great Earthquake, the Japanese government acknowledged that the enhanced GICs due to the extremely severe magnetic storms are regarded to be investigated seriously. On the other hand, as the GICs in Japan are not sufficiently investigated, we perform the basic researches about the GIE intensity map in Japan by using a modelled ground resistivity structure.

We constructed a 3-D resistivity model of the Earth surface, estimated from bathymetry and sediment thickness data. We then calculated the intensity

of the GIE based on the inferred resistivity model. Based on our work, several areas of Japan appear prone to enhanced GIEs: (1) the northeast coast of Hokkaido, along the Sea of Okhotsk; (2) the west coast of southern Hokkaido and Aomori Prefecture (Matsumae-Tsugaru area), along the Sea of Japan; (3) the northwest coast of Niigata Prefecture and Toyama Bay, on the Sea of Japan; and (4) the southwest coast of the Pacific Ocean in the Japan islands. Notably, all enhanced areas are located on the coast.

From the discussions in Fig. 6, the GIE variations in the coastline of the Japan Sea and that in the Pacific Ocean side become anti-phase. Therefore if a transformer station is located in the Japan-Sea area with enhanced GIEs (for example, Tsugaru Peninsula) and the neighboring station is located in the Pacific-Ocean side (for example, the coastline of the Iwate Prefecture), the potential difference between the two stations may be very large. Thus, the GIE map presented here can be used as a preliminary hazard map for the GIC disasters.

MT impedance vectors obtained from our modeling work are comparable to observed values in Hokkaido. In addition, we obtained MT impedances for Kanto Plain, where anthropogenic noise makes accurate field measurements impossible. The map of MT impedance vectors in Japan may provide a useful reference for electric and magnetic measurements in the future, when more detailed resistivity models become possible.

Resistivity in the crust and mantle control GIE intensity. Therefore, it is important to use fine-scale resistivity distributions in modeling work. If resistivity structure can be directly measured, the GIE map will be improved greatly. We also stress that simulated GIEs must be compared with observed values in order to validate any modeled maximum GIE map. Finally, in order to accurately estimate hazards, GIC values must be calculated using data from power line systems and transformer stations.

### Acknowledgments

The authors are grateful to M. Uyeshima of The University of Tokyo for his assistance with the computational code and discussions. We are also thankful to A. Pulkkinen of NASA for useful discussions. Figures were drawn with the Generic Mapping Tools software package [Wessel and Smith, 1998]. This

work was supported by JSPS KAKENHI Grant Number JP15H05815 (PSTEP).

Some of the results of this paper already appeared in the report of [http://www.meti.go.jp/meti\\_lib/report/2015fy/000095.pdf](http://www.meti.go.jp/meti_lib/report/2015fy/000095.pdf) (in Japanese) [METI, 2015]. This paper is a full paper describing all scientific matters obtained by the present research.

### References

- Akasofu, S. I., The development of the auroral sub-storm, *Planet. Space Sci.*, vol 12: pp 273–282, 1964.
- Amante C, and Eakins B. W., ETOPO1 1 Arc-Minute Global Relief Model: Procedures, Data Sources and Analysis. NOAA Technical Memorandum NESDIS NGDC-24. National Geophysical Data Center, NOAA. doi,10.7289/V5C8276M, 2009.
- Araki, T., Global structure of geomagnetic sudden commencements, *Planet. Space Sci.*, vol 25, pp 373–384, 1977.
- Baker D. N., Li X, Pulkkinen A, Ngwira C. M., Mays M. L., Galvin A. B., and Simunac K. D. C., A major solar eruptive event in July 2012, Defining extreme space weather scenarios. *Space Weather* vol.11, 585–591, 2013.
- Bolduc L., GIC observations and studies in the Hydro-Québec power system. *J Atmos Sol Terr Phys* vol. 64, pp 1793–1802, 2002.
- Cagniard L., Basic theory of the magnetotelluric method of geophysical prospecting. *Geophysics* vol 18, pp 605–635, 1953.
- Evans R. I., Earth's electromagnetic environment. In, Chave A, Jones A (eds.) *The Magnetotelluric method*. Cambridge Univ Press, Cambridge, 2012.
- Everett M. E., Constable S, and Constable C. G., Effects of near-surface conductance on global satellite induction responses. *Geophys J Int* vol 153(1), pp 277–286, 2003.
- Ferguson I. J., Jones A. G., Chave A. D., Case histories and geological applications, in, *The Magnetotelluric method*. ed. By Chave A. and Jones A., Cambridge Univ Press, Cambridge, 2012.
- Fujii I., Ookawa T., Nagamachi, S. and Owada T., The characteristics of geoelectric fields at Kakioka, Kanoya, and Memambetsu inferred from voltage measurements during 2000 to 2011. *Earth Planets Space* vol. 67,62. doi,10.1186/s40623-015-

- 0241-z, 2015.
- Fujiwara S. and Toh H., Geomagnetic Transfer Functions in Japan Obtained by First Order Geomagnetic Survey. *J Geomag Geoelectr* vol 48, pp 1071-1101, 1996.
- Gaunt C. T., and Coetsee G., Transformer failures in regions incorrectly considered to have low GIC-risk. Paper presented at Power Tech 2007. Inst of Electr and Electron Eng, Lausanne, Switzerland, 2007.
- Hata M., Oshiman N., Yoshimura R., Tanaka Y., and Uyeshima M., Three dimensional electromagnetic imaging of upwelling fluids in the Kyushu subduction zone, Japan. *J Geophys Res* vol 120(1), pp 1-17. doi,10.1002/2014JB011336, 2015.
- Honkura Y., Perturbation of induced electric currents by surface conductivity inhomogeneity with special reference to anomalous behavior of short-period geomagnetic variations in the Kanto Plain, Japan. *J Geomag Geoelectr* vol 37, pp 627-641, 1985.
- Kamide, Y., McPherron, R. L., Gonzalez, W. D., Hamilton, D. C., Hudson, H. S., Joselyn, J. A., Kahler, S. W., Lyons, L. R., Lundstedt, H. and Szuszczywicz, E., Magnetic Storms, Current Understanding and Outstanding Questions, in *Magnetic Storms* (eds B. T. Tsurutani, W. D. Gonzalez, Y. Kamide and J. K. Arballo), American Geophysical Union, Washington, D. C.. doi,10.1029/GM098p0001, 1997.
- Kanda W., and Ogawa Y., Three-dimensional electromagnetic imaging of fluids and melts beneath the NE Japan arc revisited by using geomagnetic transfer function data. *Earth Planets Space* vol 66,39. doi,10.1186/1880-5981-66-39, 2014.
- Kappenman J. G., An overview of the impulsive geomagnetic field disturbances and power grid impacts associated with the violent Sun-Earth connection events of 29-31 October 2003 and a comparative evaluation with other contemporary storms. *Space Weather* 3,S08C01. doi,10.1029/2004SW000128, 2005.
- Kelbert A., Schultz A., and Egbert G., Global electromagnetic induction constraints on transition-zone water content variations. *Nature* vol 460(7258), pp 1003-1006, 2009.
- Kuvshinov A., Sabaka T., and Olsen N., 3-D electromagnetic induction studies using the Swarm constellation, Mapping conductivity anomalies in the Earth's mantle. *Earth Planets Space* vol 58(4), pp 417-427, 2006.
- Laske G., and Masters G., A global digital map of sediment thickness. *EOS Trans AGU* 78,483, 1997.
- McKay A. J., Geoelectric fields and geomagnetically induced currents in the United Kingdom. Dissertation, University of Edinburgh, 2004.
- METI (Ministry of Economy, Trade, and Industry), [http://www.meti.go.jp/meti\\_lib/report/2015fy/000095.pdf](http://www.meti.go.jp/meti_lib/report/2015fy/000095.pdf) (in Japanese), 2015.
- Parkinson, W. D., The influence of continents and oceans on geomagnetic variations. *Geophys J R Astro Soc* vol.6, pp 441-449, 1962.
- Pirjola, R., (2008), Study of effects of changes of earthing resistances on geomagnetically induced currents in an electric power transmission system, *Radio Sci.*, Vol. 43, RS1004, doi,10.1029/2007RS003704, 2008.
- Pulkkinen A., Pirjola R., and Viljanen A., Statistics of extreme geomagnetically induced current events. *Space Weather* vol. 6, S07001. doi,10.1029/2008SW000388, 2008.
- Pulkkinen A., Kataoka R., Watari S., and Ichiki M., Modeling geomagnetically induced currents in Hokkaido, Japan. *Advances in Space Research* vol.46, pp 1087-1093, 2010.
- Pulkkinen A., Bernabeu E., Eichner J., Beggan C. and Thomson A. W. P., Generation of 100-year geomagnetically induced current scenarios. *Space Weather* vol. 10, S04003. doi,10.1029/2011SW000750, 2012.
- Püthe C., and Kuvshinov A., Towards quantitative assessment of the hazard from space weather. Global 3-D modellings of the electric field induced by a realistic geomagnetic storm. *Earth Planets Space* vol 65, pp 1017-1025, 2013.
- Püthe C., Manoj C. and Kuvshinov A., Reproducing electric field observations during magnetic storms by means of rigorous 3-D modelling and distortion matrix co-estimation. *Earth Planets Space* vol 66,162. doi,10.1186/s40623-014-0162-2, 2014.
- Takasu, N., Miyawaki, F., Saito, S., and Fujiwara, Y., DC excitation of transformer cores due to geomagnetically-induced currents, *IEEJB*, Vol. 113, No. 4, pp 435-444, 1993. (in Japanese)
- 高須伸夫・宮脇文彦・斎藤 達・藤原康夫, 地磁

気誘導電流による変圧器の直流偏磁場現象の検討, 電学論 B, Vol. 113, No. 4, pp 435-444, 1993.

Torta J. M., Serrano L., Regue J. R., Sanchez A. M., and Roldan E., Geomagnetically induced currents in a power grid of northeastern Spain. *Space Weather* vol.10, S06002. doi,10.1029/2012SW000793, 2012.

坪井 昭・堀内 進, 磁気嵐と電力系統, 電学誌, vol. 108, No. 3, p.p. 233-236, 1988. (in Japanese)

Tsurutani, B. T., W. D. Gonzalez, G. S. Lakhina, and S. Alex, The extreme magnetic storm of 1-2 September 1859, *J. Geophys. Res.*, vol. 108, 1268, doi,10.1029/2002JA009504, A7, 2003.

Uyeshima M., and Schultz A., Geoelectromagnetic induction in a heterogeneous sphere, a new

three-dimensional forward solver using a conservative staggered-grid finite difference method. *Geophys J Int* vol 140, pp 636-650, 2000.

Uyeshima M., Utada H., and Nishida Y., Network-magnetotelluric method and its first results in central and eastern Hokkaido, NE Japan. *Geophys J Int* vol 146, pp 1-19, 2001.

Watari S., Kunitake M., Kitamura K., Hori T., Kikuchi T., Shiokawa K., Nishitani N., Kataoka R., Kamide Y., Aso T., Watanabe Y., and Tsuneta Y., Measurements of geomagnetically induced current in a power grid in Hokkaido, Japan. *Space Weather* vol. 7, S03002. doi,10.1029/2008SW000417, 2009

Wessel P., and Smith W. H. F., New, improved version of Generic Mapping Tools released". *EOS Trans AGU* vol 79(47), p 579, 1998.

## 日本および周辺領域における地磁気誘導電場分布の数値計算

藤田 茂<sup>1,2</sup>, 藤井郁子<sup>1</sup>, 遠藤 新<sup>3</sup>, 富永博紀<sup>4</sup>

<sup>1</sup>気象大学校, <sup>2</sup>国立極地研究所, <sup>3</sup>気象庁地球環境海洋部, <sup>4</sup>東京管区気象台

2017年11月27日受領, 2017年12月14日受理, 2018年3月23日刊行

### 要 旨

日本の地磁気誘起電場 (GIE) の全国強度マップを, 数値モデリング手法を用いて求めた。地球表面近傍の電気抵抗率分布は, 地下深度と堆積物の厚さデータから推定する。GIE 強度分布は, 200, 800, および3,600秒の周期を持つ外部地磁気変化に対して計算した。GIE 強度は, 地磁気観測所における100 nT の磁気変動に対して正規化されている。GIE は主に沿岸域で大幅に増大しているように見える。加えて, 数キロメートルの内陸部まで及んでいる。現在の計算から, GIE が大幅に増強される可能性のある地域を特定する。これは, (1) 北海道オホーツク海の北東海岸域, (2) 北海道および青森県 (松前津軽地域) の日本海沿岸の西海岸域, (3) 新潟県から富山湾にかけての日本海北西部域, (4) 太平洋の南西海岸域, (5) 朝鮮半島の東海岸域である。さらに我が国の地磁気誘起電流 (GICs) を知る必要がある。しかし, 日本の電力会社は電力線のパラメータを公開していないため, 日本の GIC を計算することはできない。